Chem Catalysis

CellPress

Article

Identifying the active site of Cu/Cu_2O for electrocatalytic nitrate reduction reaction to ammonia

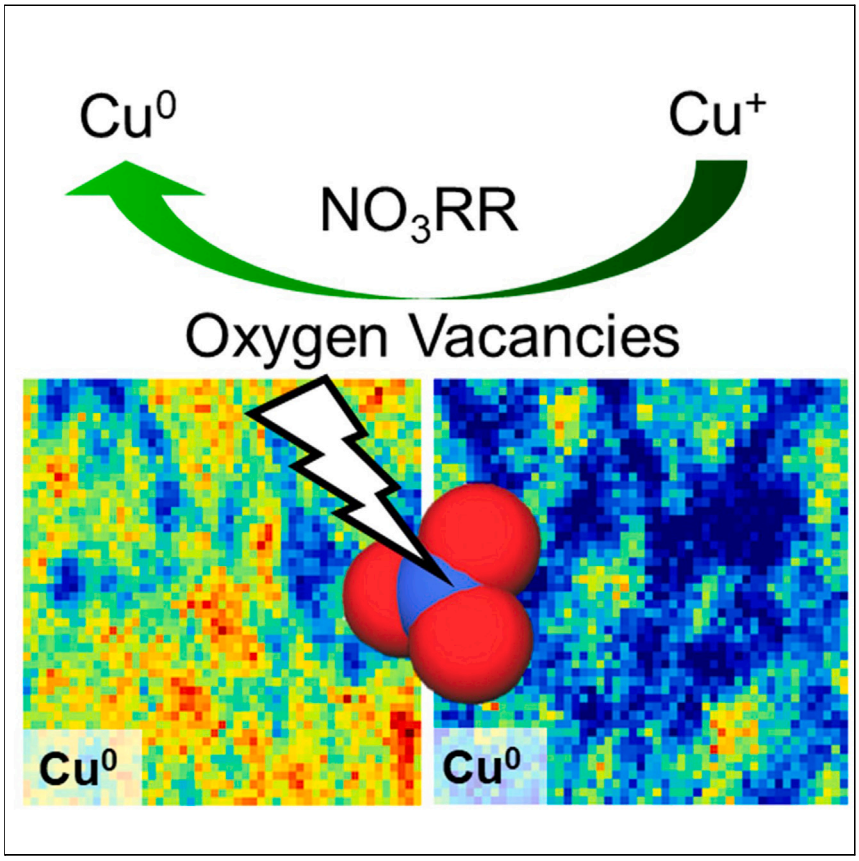

The active site of copper oxide-based electrocatalysts for nitrate electrochemical reduction to ammonia is under debate in the literature. We successfully established a potential dependence of the catalytic active site and activity of Cu/Cu_2O for nitrate electrochemical reduction to ammonia employing kinetic and *in situ* spectroscopic studies.

Gabriel F. Costa, Manuel Winkler, Thiago Mariano, ..., Cláudio F. Tormena, Nirala Singh, Raphael Nagao

snirala@umich.edu (N.S.)
nagao@unicamp.br (R.N.)

Highlights

Cu_2O electrochemically reduces during nitrate reduction to ammonia

Oxygen vacancies boost ammonia formation at lower overpotentials

Copper itself is active for ammonia production at higher overpotentials

The pH of unbuffered electrolyte increases during nitrate reduction

Costa et al., Chem Catalysis 4, 100850
January 18, 2024
https://doi.org/10.1016/j.checat.2023.100850

Chem Catalysis

CellPress

Article

Identifying the active site of Cu/Cu_2O for electrocatalytic nitrate reduction reaction to ammonia

Gabriel F. Costa,[1,2] Manuel Winkler,[1,3] Thiago Mariano,[1,3] Maria R. Pinto,[1,4] Igor Messias,[1] João B. Souza, Jr.,[5] Itamar T. Neckel,[6] Maria F.C. Santos,[1] Cláudio F. Tormena,[1] Nirala Singh,[2,*] and Raphael Nagao[1,3,7,*]

SUMMARY

Copper oxide-derived electrocatalysts are reported to have high activity and selectivity for nitrate electrochemical reduction reaction (NO_3RR) to ammonia. However, the cause underlying their enhanced NH_3 formation remains unclear. We measure the NO_3RR activity of differently pre-reduced Cu/Cu_2O catalysts and compare them to metallic Cu to identify the active site for NO_3RR to ammonia in sodium sulfate electrolyte. Using unbuffered electrolyte, catalyst kinetic performance is similar to the alkaline one (pH 12) due to pH increases during NO_3RR. Higher pH values improve catalyst performance for NO_3RR to NH_3 compared to electrolyte buffered at pH 5.8. Using *in situ* spectroscopies, we detect that Cu_2O reduces at −0.6 V vs. standard hydrogen electrode (SHE) and detect hydroxylamine, a NO_3RR intermediate, from −0.7 V to −1.0 V vs. SHE. We propose that oxygen vacancies promote NO_3RR to ammonia from −0.6 to −0.77 V vs. SHE, while copper is the active site at −1.1 V vs. SHE.

INTRODUCTION

The synthesis of ammonia via Haber-Bosch (HB) process, obtained from nitrogen (N_2) catalytic hydrogenation, has increased the availability of fertilizers and allowed mass production of food to support population growth.[1,2] The use of fossil fuels as energy and hydrogen sources for ammonia synthesis makes HB the largest carbon dioxide emitting chemical industry process.[3] Additionally, HB has caused an imbalance in the global nitrogen cycle due to the production of ammonia from a non-reactive source (N_2), fixing 10^8 tons of nitrogen into reactive species per year.[4,5] Among nitrogenous contaminants, nitrate is the main pollutant of wastewater and the most oxidized species.[5] The accumulation of nitrate (NO_3^-) in ecosystems is leading to harmful consequences for the environment and human health.[2,6] For example, the consumption of nitrate found in drinking water can be attributed to the development of diseases such as cancer and methemoglobinemia.[2]

To tackle this issue, NO_3^- electrochemical reduction reaction (NO_3RR) to ammonia (NH_3) can be an alternative for both wastewater treatment and sustainable ammonia synthesis.[6,7] Making this reaction viable could also help decarbonize ammonia production and convert an important pollutant from water streams (NO_3^-) into a valuable product (NH_3).[3,6] However, NO_3RR can lead to the production of a large range of nitrogenous compounds, such as NO_2^-, NO, N_2O, N_2, and NH_3.[5,8] The

THE BIGGER PICTURE

The intensive use of fertilizers enabled by Haber-Bosch hydrogenation of N_2 led to the accumulation of reactive nitrogen species in water streams. Nitrate (NO_3^-), the most oxidized nitrogen contaminant, is harmful for both environmental and human health. The electrochemical conversion of nitrate into valuable products, such as ammonia, is a promising alternative to overcome this problem. Among the catalysts used for this reaction, copper-based ones, especially its oxides, are widely studied due to their favorable charge transfer between the metal and nitrate species. Our work relies on an ongoing puzzle in the literature regarding the active site of copper oxides for nitrate electrocatalytic reduction to ammonia.

distribution of these products is based on the catalyst's role in the adsorption and stabilization of intermediates during the reaction.[8,9] Thus, understanding how emergent catalysts act in the production of ammonia from NO_3RR is fundamental to designing these materials, preferentially based on highly available and non-noble metals.[10] The highly occupied d-band of some metals, such as Cu, Ag, and Pt, has similar energy levels to the lowest unoccupied molecular π* orbital (LUMO π*) of NO_3^-, and this energy alignment can promote electron transfer.[9,11] Among these metals, Cu has the fastest rate of conversion of NO_3^- to NO_2^-, the rate-determining step for NO_3RR, and can further reduce NO_2^- to other products including NH_3.[12]

Copper oxides combined with Cu phases are also studied due to their noteworthy enhancement of performance parameters for NH_3 synthesis, such as Faradaic efficiency and yield rate compared to purely metallic catalysts.[13–22] Moreover, there are also works that report the interface of Cu_2O with other transition metals, such as Pd and Ni, as potential active sites that boost NO_3RR to NH_3.[23,24] However, the active site of these materials to catalyze the formation of ammonia from NO_3RR is still under debate. Considering the copper Pourbaix diagram,[25] copper oxide can be electrochemically reduced into metallic copper depending on the electrolyte pH and applied overpotential.[16,17,26,27] Copper oxide-based catalysts reported in the literature are more efficient for NO_3RR to ammonia under potential and pH conditions in which oxide species are expected to be reduced.[25] To identify the role of the oxide and reduced copper species for NO_3RR, it is necessary to determine the structure and identity of these catalysts at the potential under which NO_3^- is adsorbed and reduced.[27] Besides that, NO_3RR to NH_3 is a highly proton-consuming reaction that can lead to a significant pH change during the electrolysis, which can impact the performance of the catalyst when employing non-buffered electrolytes.[28]

Wang et al.[13] and Zhao et al.[14] attribute the enhancement of copper oxides compared to copper to the ability of the interface between Cu and Cu_2O to promote hydrogenation of *NO intermediates and to suppress the hydrogen evolution reaction (HER). Yin et al.[15] evaluate Ag/Cu_2O hybrid nanoparticles for NO_3RR and found that the interaction between the oxide and metal phases acts as an adsorption site that inhibits the formation of *NOH and boosts the generation of *N. On the other hand, Daiyan et al.[16] and Yuan et al.[17] attribute the activity of Cu/Cu_2O catalyst for NO_3RR to the presence of oxygen vacancies in the lattice from the reduced copper oxides. They propose that these oxygen vacancies can stabilize key intermediates for NH_3 production. Contrary to the previous hypotheses, Li et al.[18] and Song et al.[19] argue that copper species are intrinsically active for NO_3RR, and the reduction of its oxides is not preponderant for the catalyst performance. Recently, Zhou et al.[20] reported a dependence of the applied potential on the role of $Cu\text{-}Cu_2O$ nanocubes in product distribution for NO_3RR. They proposed that the oxide-metal interface catalyzes NO_2^- formation at lower overpotentials (>−0.6 V vs. reversible hydrogen electrode [RHE]), and oxide-derived Cu is more active for NH_3 production at higher overpotentials (<−0.6 V vs. RHE). Clearly, there is not currently a consensus on the active site for Cu/Cu_2O composites for NO_3RR.[16,17,26,28]

In this work, we seek to identify the active site of copper oxide-based electrocatalysts for NO_3RR to NH_3 in different potential windows. We electrochemically synthesize a composite containing both Cu and Cu_2O to evaluate the interface between them as a potential active site for NO_3RR to ammonia. By employing different durations of a pre-reduction step to the catalyst before measuring the kinetics, we probe two other possible active sites: oxygen vacancies and oxide-derived Cu. During NO_3RR, we detect an alkaline shift in the pH of the unbuffered electrolyte from pH

[1]Institute of Chemistry, University of Campinas, Campinas 13083-862, São Paulo, Brazil

[2]Department of Chemical Engineering, University of Michigan, Ann Arbor, MI 48109-2136, USA

[3]Center for Innovation on New Energies, University of Campinas, Campinas 13083-084, São Paulo, Brazil

[4]Leiden Institute of Chemistry, Leiden University, 2300 RA Leiden, the Netherlands

[5]Brazilian Nanotechnology National Laboratory (LNNano), Brazilian Center for Research in Energy and Materials (CNPEM), Campinas 13083-100, São Paulo, Brazil

[6]Brazilian Synchrotron Light Laboratory (LNLS), Brazilian Center for Research in Energy and Materials (CNPEM), Campinas 13083-100, São Paulo, Brazil

[7]Lead contact

*Correspondence: snirala@umich.edu (N.S.), nagao@unicamp.br (R.N.)

https://doi.org/10.1016/j.checat.2023.100850

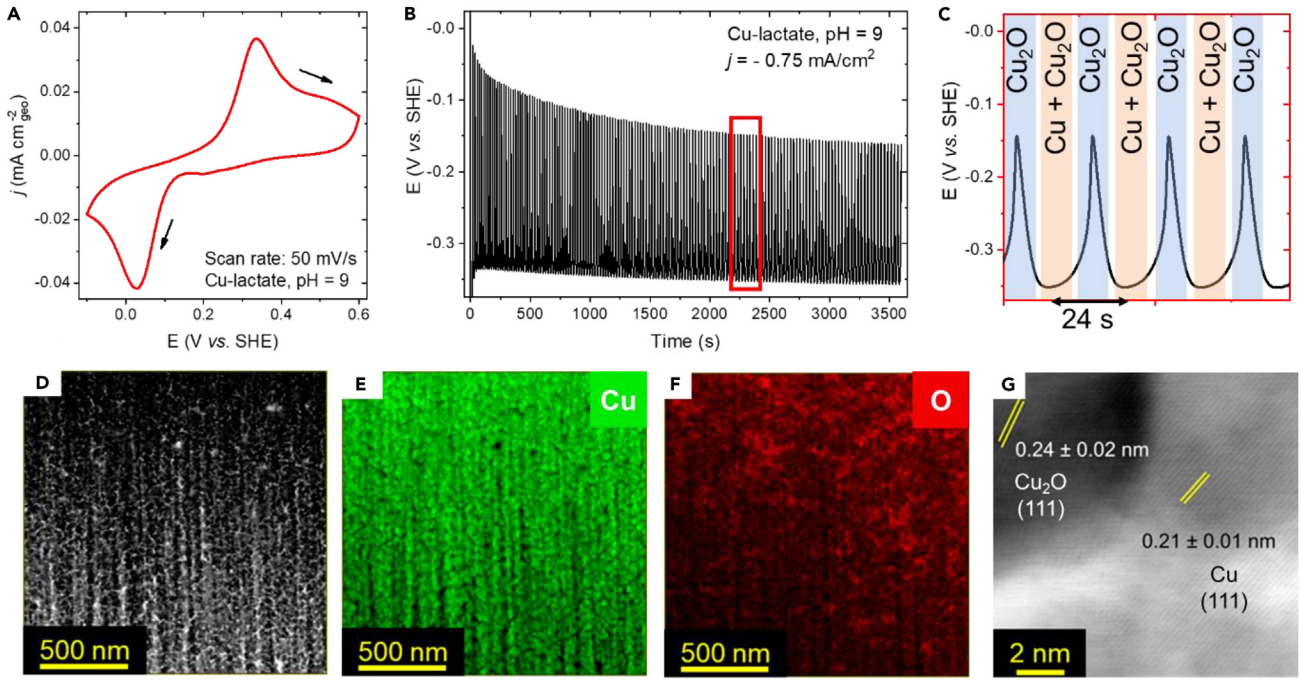

Figure 1. Synthesis and characterization of Cu/Cu_2O composite

(A) Cyclic voltammetry at 0.05 V s^{-1} from −0.1 to 0.6 V (vs. SHE) for Cu(II)-lactate system: [$CuSO_4$] = 0.5 mol L^{-1}, [lactate] = 2.5 mol L^{-1}, pH 9.0. Working electrode is a gold plate.

(B) Composite deposition on the gold plate by chronopotentiometry at −0.75 mA cm^{-2} for 1 h.

(C) Red rectangle indicates the region highlighted in (B), (indicating the oscillation region in which Cu_2O and Cu + Cu_2O are deposited.

(D–F) TEM image (D) of an FIB-sampled cross-section lamella extracted from Cu/Cu_2O film with the respective EDS maps of (E) copper and (F) oxygen.

(G) High-resolution TEM image indicating interplanar distances for the darker (0.24 nm) and brighter region (0.21 nm) correlated to Cu_2O (111) and Cu (111) phases, respectively.

5.8 to approximately 12. We demonstrate that the kinetics of NO_3RR to NH_3 in the unbuffered electrolyte are more similar to alkalized electrolytes that begin at pH 12, rather than buffered electrolytes that remain at pH 5.8 throughout the reaction. We combine *ex situ* and *in situ* spectroscopic and microscopic characterizations to assess how cathodic potentials modify the catalyst and show evidence of Cu_2O reduction, as well as structural changes of the catalyst. By considering the kinetics and characterization as well as previous reports in the literature on Cu and Cu_2O composites, we postulate that under low overpotential (−0.6 to −0.77 V vs. standard hydrogen electrode [SHE]), oxygen vacancies are the active site for NO_3RR to NH_3, whereas at higher overpotentials (−1.1 V vs. SHE), Cu is the active site.

RESULTS AND DISCUSSION

Electrochemical deposition and characterization of Cu/Cu_2O catalyst

We synthesized a nanostructured composite of Cu and Cu_2O by galvanostatic electrodeposition using a Cu(II)-lactate electrolyte at pH 9 to study the role of the metal-oxide interface for NO_3RR.[29,30] Alternated deposition of metallic Cu and semiconductor Cu_2O can be obtained by spontaneous potential oscillations in Cu(II)-lactate system that emerge under specific conditions of pH (from 8.0 to 10.5) and applied current density (from 0.025 to 8.0 mA cm^{-2}).[31] Figure 1A shows the voltammetric profile of a gold electrode in the Cu(II)-lactate electrolyte, where oxidation and reduction peaks for Cu are at 0.33 and 0.02 V vs. SHE, respectively.[29,30] We electrodeposit the Cu/Cu_2O composite at −0.75 mA cm^{-2}, where spontaneous potential

oscillations between −0.35 and −0.17 V vs. SHE occur (Figure 1B).[29,30] These oscillations allow the alternating deposition of Cu_2O at less negative potentials and a composite containing both Cu and Cu_2O at more negative potentials, as shown in the zoomed Figure 1C, obtained from the highlighted red rectangle at the time series (Figure 1B).[30]

Using focused ion beam (FIB) sampling and transmission electron microscopy (TEM), we characterized a cross-section lamella of the Cu/Cu_2O deposit, enabling us to assess the distribution of elements and to identify distinct domains corresponding to Cu and Cu_2O. We show the bright-field TEM image of the electrodeposited sample in Figure 1D, where we identify a porous structure along the deposit. Figures 1E and 1F display the energy dispersive X-ray spectroscopy (EDS) maps for the distribution of Cu and O, and we detect the formation of domains with higher and lower amounts of oxygen, likely related to Cu_2O and Cu, respectively. We confirm with high-resolution TEM (Figure 1G) the formation of these domains, in which we measured the lattice distances attributed for Cu (111) and Cu_2O (111) regions: 0.21 and 0.24 nm respectively, in accordance with the literature.[32] However, under electrochemical conditions, the oxide structures may reduce, and we further characterize our sample as discussed below.

Kinetic evaluation of pre-reduction steps on Cu/Cu_2O for electrochemical NO_3RR to ammonia

We compare the kinetic behavior of Cu-Cu_2O interface, oxygen vacancies, and pure copper as potential active sites for NO_3RR to ammonia, revealing that oxygen vacancies are active at lower overpotentials (−0.6 to −0.77 V vs. SHE), and copper exhibits intrinsic activity at higher overpotentials (−1.1 V vs. SHE). In Figure 2A, we compare the partial current densities to NH_3 in unbuffered Na_2SO_4 electrolyte for the as-prepared Cu/Cu_2O catalyst, a Cu/Cu_2O catalyst that has been partially reduced (10 min of pre-reduction at −1.0 V vs. SHE), and heavily reduced Cu/Cu_2O catalyst (10 h of pre-reduction at −1.0 V vs. SHE). We also include the performance of pure metallic Cu plate deposited on a silicon wafer. We choose sodium sulfate as supporting electrolyte, widely used to study NO_3RR to ammonia,[13,14,21,33] since most of nitrate-contaminated water streams are unbuffered neutral solutions.[28,34] We discuss the effect of pH changes due to NO_3RR in detail in the next section. The as-prepared and partially reduced catalysts have similar activity over the entire potential range tested. We propose that this phenomenon is due to the rapid Cu_2O reduction and oxygen vacancy formation under nitrate reduction conditions. As such, the 10 min of pre-reduction do not have a significant effect when compared to the reduction during the reaction itself (NO_3RR results are after 10 min of electrolysis). If under these conditions there is a significant reduction of Cu_2O, it suggests that Cu and Cu_2O interfaces would not be present, and thus the interface between Cu and Cu_2O is not the active site for NO_3RR to NH_3 from −0.6 to −1.1 V vs. SHE. We investigate the effect of the reduction on the structure of the catalyst in later sections to test this hypothesis. We detect this enhancement in NH_3 formation at oxygen vacancies utilizing non-buffered electrolyte, in which a significant pH shift during NO_3RR occurs, impacting the catalyst/electrolyte interface, which we discuss in the next section.

The metallic copper and 10-h-reduced Cu/Cu_2O exhibit lower activity compared to the less-reduced catalysts for NO_3RR at −0.6 and −0.77 V vs. SHE (inset in Figure 2A), which indicates that Cu is not the active site for NO_3RR to NH_3 at lower overpotentials. However, the 10-h-reduced catalyst and metallic Cu demonstrate higher activity at higher overpotentials (−1.1 V vs. SHE) than the as-prepared and

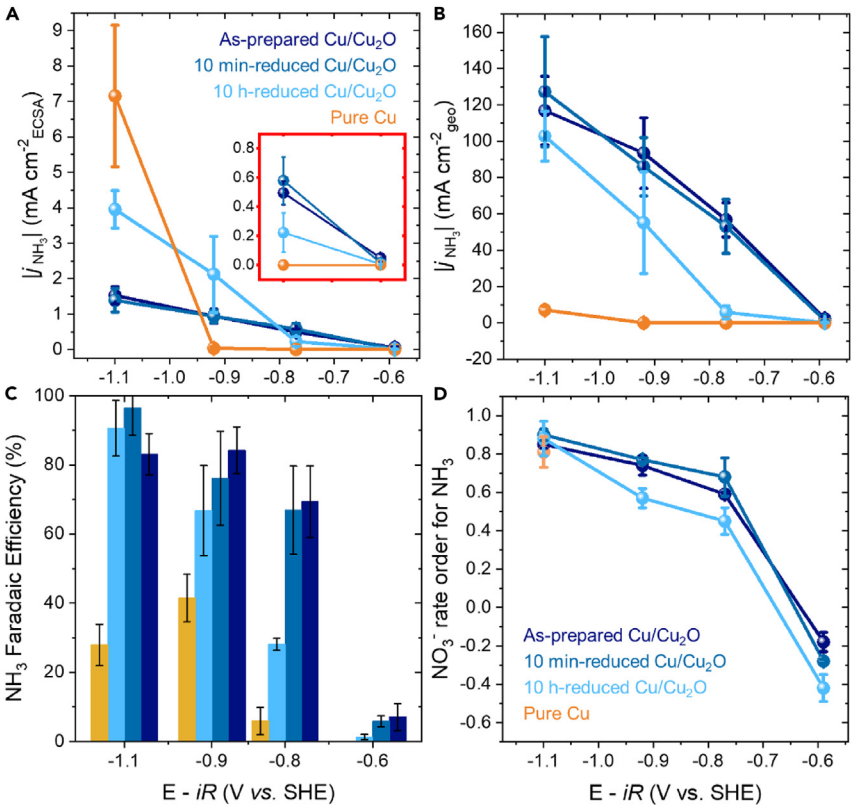

Figure 2. Kinetic evaluation of differently reduced Cu/Cu_2O

(A–C) NH_3 partial current densities calculated by (A) ECSA and (B) geometric area and (C) Faradaic efficiencies toward NH_3 obtained from 10-min electrolysis with $[NaNO_3]$ = 50 mmol L^{-1} for as-prepared Cu/Cu_2O composite, 10-min-reduced and 10-h-reduced Cu/Cu_2O at −1.0 V vs. SHE. (D) Relationship between nitrate rate order and applied potential extracted from ammonia partial current density (j_{NH3}) for the as-prepared Cu/Cu_2O composite, 10-min-reduced and 10-h-reduced Cu/Cu_2O at −1.0 V vs. SHE. Data were extracted from 10-min chronoamperometric electrolysis with electrolyte containing 0.5 mol L^{-1} Na_2SO_4 (pH_0 = 5.8) and 5, 10, and 50 mmol L^{-1} $NaNO_3$ stirred at 700 rpm. All error bars denote standard deviation from the average of three (n = 3) separate measurements.

10-min-reduced Cu/Cu_2O. The increased activity of the most reduced Cu/Cu_2O and pure Cu at larger overpotential suggests that under these conditions, Cu is intrinsically active for NO_3RR to ammonia. We refer to the 10-h-reduced Cu/Cu_2O as oxide-derived Cu below. Considering that 10-h-reduced Cu/Cu_2O presents a rougher surface than pure Cu, the fact that flat metallic Cu is more active than oxide-derived Cu can be related to the hampered mass transport of NO_3^- toward the active site in a rough structure.[35] Based on our findings, we suggest that at −1.1 V vs. SHE, copper itself is the active site for NO_3RR to ammonia.

By comparing the geometric current density to the current density normalized by the electrochemically active surface area (ECSA), we see that a major difference in the Cu/Cu_2O catalysts compared to pure Cu is their higher surface area, although there are still inherent differences in activity. Figure 2B shows the current density normalized to the geometric area of the electrode, in which the highly roughened electrode area for the Cu/Cu_2O catalysts leads to greater ammonia production. We emphasize that this does not mean that they are more active than pure Cu on a per active site basis. In fact, at −1.1 V vs. SHE, when normalizing to the ECSA, Cu has a higher

intrinsic activity than Cu_2O-based materials (Figure 2A). In Figure S3, we show that double layer capacitance (C_{dl}), which was employed to calculate the ECSA (Figure S2), rapidly decreases by applying reductive potential. We attribute this decrease to Cu_2O reduction, which suppresses the pseudo-capacitance from the metal-oxide interface that contributes to a larger measured capacitance,[36] and structural changes that occur after electrolysis, which will be discussed in following sections. We also measured the pure Cu C_{dl} before and after electrolysis (Figure S4), and the values were the same, indicating that Cu ECSA remains the same after electrolysis. For this reason, we considered the C_{dl} measured after electrolysis when calculating ECSA.

Partial reduction of copper oxides improves the catalyst Faradaic efficiencies toward NH_3 at low overpotentials (−0.6 to −0.77 V vs. SHE), and differently reduced Cu/Cu_2O catalysts are equally efficient at higher ones (−0.93 to −1.1 V vs. SHE) and more selective than metallic copper (Figure 2C). The selectivity trends of differently reduced Cu/Cu_2O are in accordance with the catalysts' activities and agree with the potential dependence for active sites previously reported (Figure 2A). However, pure Cu is less selective toward ammonia than oxide-derived Cu. The difference between them can be associated either to distinct proportions of Cu lattice facets,[37] which impacts the distribution of active sites, or possible grain boundaries formed after Cu_2O reduction in the catalyst lattice, serving as potential active sites for NO_3RR.[38] The remaining Faradaic efficiency may be related to HER, considering that we do not detect considerable amounts of NO_2^- after electrolysis at −1.1 V vs. SHE (Figure S6), and we observe the formation of bubbles during the reaction. Also, different Cu_2O facets lead to differently active Cu surfaces, with Cu derived from Cu_2O (111) more active than the surface derived from Cu_2O (100), as reported by Anastasiadou et al.[22]

The trends of reaction rate orders were similar for as-prepared and partially reduced Cu/Cu_2O, but oxide-derived Cu exhibited slightly lower rate orders from −0.6 to −0.93 V vs. SHE, indicating that for this potential window, increasing NO_3^- concentration impacts less the production of ammonia for Cu. At −1.1 V vs. SHE, the NO_3^- rate orders for ammonia are similar, suggesting that NH_3 activity of differently reduced Cu/Cu_2O and metallic Cu is uniformly influenced by increasing nitrate concentration. We extracted the NO_3RR rate orders for NH_3 from ammonia partial current densities (Figure 2D) by varying NO_3^- concentration from 5 to 50 mmol L^{-1} and obtained from the slope of $\log(-j_{NH3})$ vs. $\log([NO_3^-])$. For metallic copper, we extract the rate order only for −1.1 V vs. SHE, due to the below quantifiable amount of NH_3 produced at lower nitrate concentrations. At −0.6 V vs. SHE, the nitrate rate order for ammonia production was negative for the three tested catalysts. This negative reaction order can be attributed to the fact that at −0.6 V vs. SHE, other products form at high rates than NH_3, primarily NO_2^- (Figures S5 and S6), even with increasing total current with higher nitrate concentration. Consequently, as NO_3^- concentration increases, a greater number of species become available to be reduced, but these products are not subsequently converted into NH_3, causing the ammonia production rate to decrease.

Effect of pH changes on non-buffered electrolyte

We detect an increase of the catholyte pH after 10-min electrolysis when employing non-buffered 0.5 mol L^{-1} Na_2SO_4 as supporting electrolyte, shifting from 5.8 to alkaline levels (10.9–12.0), as indicated by the black arrows in Figure 3A. As discussed above, sodium sulfate is frequently used to study NO_3RR to NH_3[13,14,21,33] since most nitrate-contaminated water streams are unbuffered neutral solutions.[28,34]

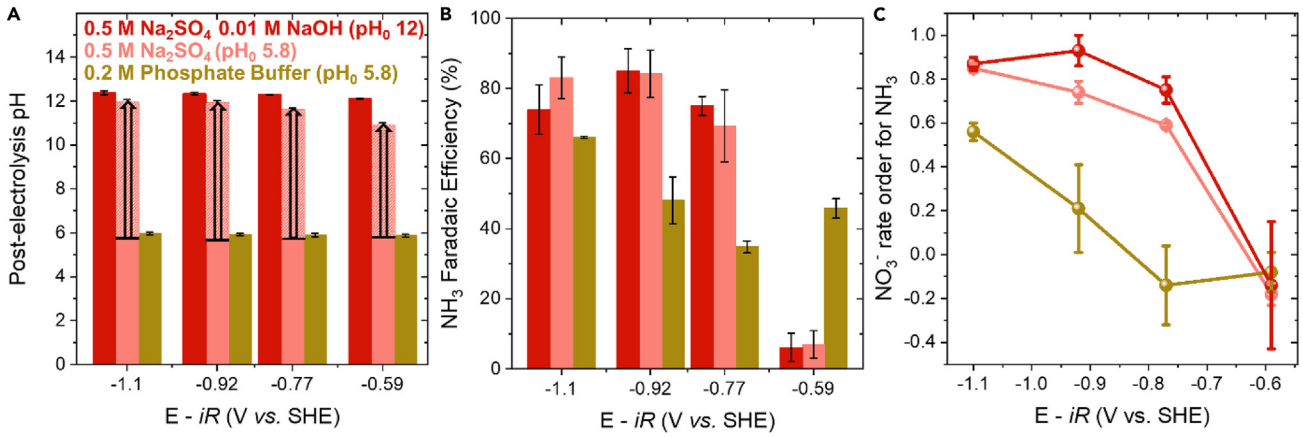

Figure 3. pH shift during electrolysis and its influence on NO_3RR to ammonia

(A) Post-electrolysis pH values and (B) NH_3 Faradaic efficiencies for alkalized (dark red), non-buffered (light red) 0.5 mol L^{-1} sodium sulfate, and 0.2 mol L^{-1} phosphate buffer (golden) electrolytes in function of applied potential for 10-min electrolysis, 50 mmol L^{-1} $NaNO_3$, and stirring rate at 700 rpm. Black arrow and shaded area in (A) indicate the pH shift in non-buffered electrolyte.

(C) Relationship between nitrate rate orders for ammonia production and applied potential. Data were extracted from chronoamperometric using the as-prepared Cu/Cu_2O catalyst as working electrode for 10-min electrolysis varying [NO_3^-] from 5 to 50 mmol L^{-1}, stirred at 700 rpm. All error bars denote standard deviation from the average of three (n = 3) separate measurements.

Because of this pH change, we report the voltage in V vs. SHE, except where noted specifically. The electrochemical conversion of NO_3^- to NH_3 requires the consumption of 8 mol of H^+ for each mole of NO_3^-,[7] which increases the pH of the electrolyte, a key variable that impacts the reaction mechanism and consequently the catalyst performance. We compared the post-electrolysis pH of the catholyte utilizing non-buffered electrolyte with 0.2 mol L^{-1} phosphate buffer (PB) at pH 5.8 and alkalized 0.5 mol L^{-1} Na_2SO_4 at pH 12. For both the buffered and alkalized electrolyte, we did not detect any significant pH shift after electrolysis (Figure 3A, dark red and golden bars respectively).

The unbuffered electrolyte (used for the data in Figure 2 and in the sections below) exhibits stronger similarity to the alkalized, non-buffered electrolyte than to the PB at pH 5.8. We found that the Faradaic efficiencies toward ammonia are notably higher for alkaline and non-buffered electrolytes from −0.77 to −1.1 V vs. SHE (Figure 3B). These trends indicate that our unbuffered electrolyte rapidly alkalizes (confirmed by pH vs. time profile in Figure S7), thereby contributing to an enhanced catalyst performance for NH_3 production from NO_3RR. This pH shift could not be attributed only to the weak capacity of the Nafion 117 membrane to exchange protons, considering that we detected a quick pH shift (from 5.8 to 10 after 1-min electrolysis) also when a one-compartment cell was used. NO_3^- rate orders for NH_3 for alkaline electrolyte (dark red line in Figure 3C) are higher than the ones obtained in buffer neutral media (golden line in Figure 3C) for the same potential range. The obtained trend for nitrate rate order using unbuffered 0.5 mol L^{-1} Na_2SO_4 electrolyte (light red line in Figure 3C) mirrors the alkaline one (dark red line in Figure 3C), which suggests that the alkalinization of the electrolyte occurs rapidly. We demonstrate that even when the applied potentials are plotted versus RHE, the rate orders for buffer electrolyte at pH 5.8 are lower than for non-buffered and alkalized Na_2SO_4 electrolytes ones (Figure S8). We also detect a peak shift attributed to Cu_2O reduction in voltammetries recorded in the absence of nitrate from −0.6 to −0.9 V vs. SHE when PB is employed in comparison with 0.5 mol L^{-1} Na_2SO_4 (Figure S9). Pérez-Gallent and coworkers[37] reported the relationship between pH and reaction mechanism for NO_3RR at single-crystal Cu. In acidic media, NO and NH_4^+ are formed, while for

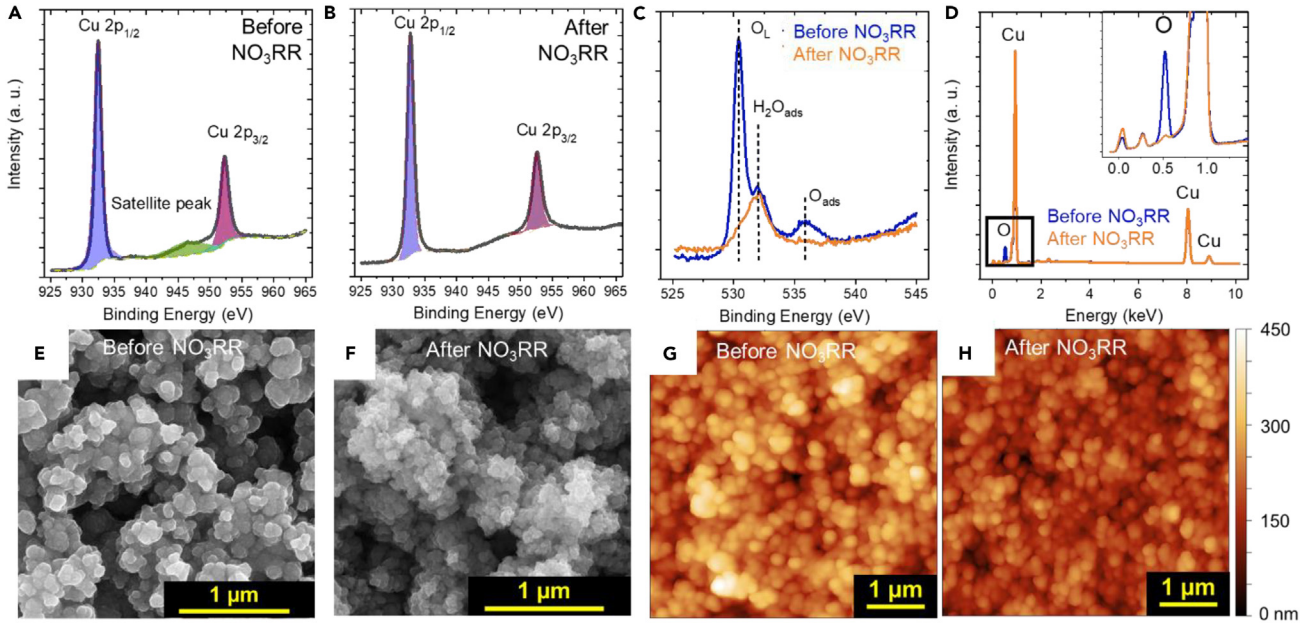

Figure 4. Cu/Cu_2O composite characterizations before and after electrochemical NO_3RR

(A–B) Copper and (C) oxygen XPS spectra for Cu/Cu_2O: before (A, blue line in C) and after (B, orange line in C) NO_3RR.

(D) EDS spectra for the catalyst before and after NO_3RR (blue and orange lines respectively) identifying the peaks related to Cu and O. Inset highlights the peak related to oxygen species.

(E–H) Scanning electron microscopy images (E and F) and atomic force microscopy roughness maps (G and H) before (E and G) and after (F and H) NO_3RR. Electrolysis conditions: 1-h electrolysis at −0.77 V vs. SHE; electrolyte containing 0.5 mol L^{-1} Na_2SO_4 and catholyte with addition of 2.35 mmol L^{-1} $NaNO_3$.

alkaline media, NO_3RR leads to the production of NO_2^- and NH_2OH. Thus, the differences between NH_3 selectivity and NO_3^- rate orders trends for PB and Na_2SO_4 indicate different reaction mechanisms or rate-determining steps for NO_3RR depending on the electrolyte pH.

Identifying structural changes in the catalyst

We detect the consumption of Cu_2O in catalyst lattice after 1-h electrolysis at −0.77 V vs. SHE by *ex situ* spectroscopies. Copper X-ray photoelectron spectra (XPS) for Cu_2O typically presents a satellite peak centered at 948 eV,[13] related to Cu^+ species. We detect this peak from the catalyst surface before electrolysis (Figure 4A) and demonstrate its absence after NO_3RR (Figure 4B), indicating the reduction of Cu_2O during electrolysis. We attribute three peaks for oxygen 1s core level in the XPS spectra: 530.4 eV related to lattice oxygen, 531.9 eV attributed to oxygen atoms from chemisorbed H_2O molecules,[39] and 535.9 attributed to adsorbed oxygen atoms.[40] We show the removal of lattice oxygen through the absence of the peak centered at 530.4 eV in the oxygen XPS spectra after NO_3RR. This decrease in lattice oxygen indicates that copper oxides species are reduced during electrolysis (Figure 4C). We show the EDS spectra from the composite before and after NO_3RR in Figure 4D, and the significant diminishment of the peak related to oxygen species at 0.52 keV (inset on Figure 4D) confirms the reduction of Cu_2O during NO_3RR.

We identify differences in the electrocatalyst structure after NO_3RR at −0.77 V vs. SHE. The surface of the as-prepared catalyst shown by scanning electron microscopy in Figure 4E presents nanometric rounded structures with cavities between them. The corners of the catalyst surface after NO_3RR are significantly smoothed after

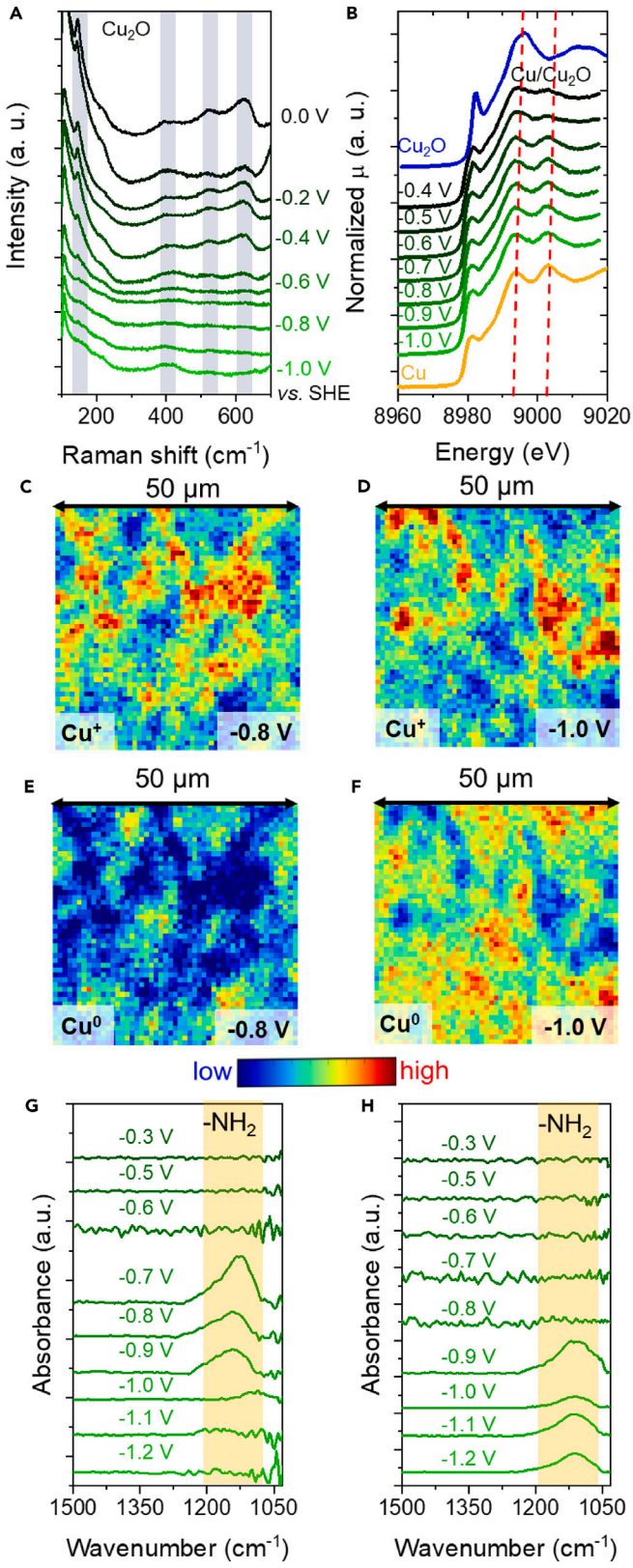
A
Cu2O
0.0 V
-0.2 V
-0.4 V
-0.6 V
-0.8 V
-1.0 V
vs. SHE
Intensity (a. u.)
200
400
600
Raman shift (cm-1)
B
Cu/Cu2O
Cu2O
-0.4 V
-0.5 V
-0.6 V
-0.7 V
-0.8 V
-0.9 V
-1.0 V
Cu
Normalized μ (a. u.)
8960
8980
9000
9020
Energy (eV)
C
50 μm
Cu+
-0.8 V
D
50 μm
Cu+
-1.0 V
E
50 μm
Cu0
-0.8 V
F
50 μm
Cu0
-1.0 V
low
high
G
-NH2
-0.3 V
-0.5 V
-0.6 V
-0.7 V
-0.8 V
-0.9 V
-1.0 V
-1.1 V
-1.2 V
Absorbance (a.u.)
1500
1350
1200
1050
Wavenumber (cm-1)
H
-NH2
-0.3 V
-0.5 V
-0.6 V
-0.7 V
-0.8 V
-0.9 V
-1.0 V
-1.1 V
-1.2 V
Absorbance (a.u.)
1500
1350
1200
1050
Wavenumber (cm-1)

Figure 5. *In situ* spectroscopic characterizations

(A and B) *In situ* Raman (A) and Cu K-edge punctual XANES (B) spectra for Cu/Cu_2O with 0.1 mol L^{-1} $NaNO_3$ and 0.5 mol L^{-1} Na_2SO_4. Peaks related to Cu_2O species from Raman spectra are highlighted: 145 cm^{-1}, 415 cm^{-1}, 520 cm^{-1}, and 630 cm^{-1} in (A). Cu XANES spectra peaks related to lattice scattering are highlighted (red dotted lines) in (B).

(C–E) Distribution of Cu oxidation states; XANES maps for (C and D) Cu^+ and (E and F) Cu^0 species of 50 × 50 μm area of the catalyst obtained at (C and E) −0.8 and (D and F) −1.0 V vs. SHE under the same electrolyte conditions of punctual XANES spectra. *In situ* FTIR spectra for (G) Cu/Cu_2O and (H) Cu, electrolyte containing 0.1 mol L^{-1} $NaNO_3$ and 0.5 mol L^{-1} Na_2SO_4. Peak centered at 1,111 cm^{-1} related to -NH_2 from NH_2OH is highlighted in yellow.

NO_3RR (Figure 4F). The average roughness determined from atomic force microscopy (AFM) decreased from 222.5 nm (Figure 4G) before NO_3RR to 173.1 nm (Figure 4H) after. We also probe the surface contact potential with Kelvin probe AFM (Figure S10), allowing us to confirm that the identity of the material changes after NO_3RR, since the average contact potential measured from same sized areas changed from 0.1957 to 0.038 V before and after NO_3RR respectively. Anastasiadou et al.[22] also reported morphological changes in Cu_2O film after NO_3RR, attributed to the reduction and dissolution of copper species during the electrolysis.

The role of Cu_2O reduction in NO_3RR to ammonia

We demonstrate through *in situ* spectroscopies that copper oxide reduces at less cathodic potentials than the potentials at which NO_3RR to ammonia occurs. Voltammetry in the absence of nitrate presents a peak centered at −0.6 V vs. SHE, which can be attributed to Cu_2O reduction (blue dotted line, Figure S9). We observe higher rates of NO_3RR to ammonia from −0.77 V vs. SHE (Figure 2D), which means that copper oxide reduces concomitantly with NH_3 production. We use *in situ* Raman spectroscopy to track the presence of Cu_2O in the catalyst lattice at different applied potentials, in which four major peaks were identified: two peaks centered at 145 and 630 cm^{-1} related to infrared active mode F_{1u} (T_{15}), one weak peak at 415 cm^{-1} attributed to multiphoton process, and one at 520 cm^{-1} related to Raman allowed mode $^3T'_{25}$ (F_{2g}).[41] These peaks related to copper (I) oxide gradually diminish from −0.6 to −1.0 V vs. SHE, which confirms that Cu_2O reduces at −0.6 V vs. SHE.

In situ Cu *K*-edge X-ray near edge spectroscopy (XANES) spectra (Figure 5B) also support that Cu_2O reduces by the emergence of two well-defined peaks at 8,993.5 and 9,003 eV[42] from −0.6 V vs. SHE to −1.0 V vs. SHE. We compared the *in situ* XANES spectra of as-prepared Cu/Cu_2O catalyst to the spectra of pure Cu_2O and Cu (blue and orange lines respectively). For Cu K-edge XANES spectra, we attribute the white line peak centered around 8,980.5 eV for the transition *1s* → *4p*.[43] We detect two peaks centered in 8,993.5 and 9,003 eV for Cu foil XANES spectra (red dotted lines in Figure 5B), related to scattering from first and second coordination shells of Cu fcc metal lattice.[43] The post-edge peaks related to Cu lattice scattering become better defined from −0.6 to −1.0 V vs. SHE, which indicates that the catalyst lattice is transitioning from a mixture of Cu/Cu_2O to metallic Cu at this potential range. These results are in accordance with the copper Pourbaix diagram, in which the transition from Cu_2O to metallic copper is expected between the potential range of 0.2 to −0.5 V vs. SHE, depending on the electrolyte pH.[25]

We demonstrate that at −1.0 V vs. SHE, the amount of Cu^0 species in the catalyst lattice increases significantly, attributed to the transition of Cu oxidation state from +1 to 0. We extract *in situ* maps of Cu^+ and Cu^0 species of 2,500 μm^2 catalyst (500 nm of pixel size) area at −0.8 and −1.0 V vs. SHE using principal components analysis (PCA) through the stack of X-ray fluorescence (XRF) images acquired over

the Cu *K*-edge XANES spectra of the Cu/Cu_2O (Figures 5C–5F). More detailed information about maps acquisition is described in the experimental procedures section.[44] From −0.8 to −1.0 V vs. SHE, the amount of Cu^+ in the catalyst decreases, shown by the transition from orange to blue/green pixels (Figures 5C and 5D). The quantity of Cu^0 species increases significantly from −0.8 to −1.0 V vs. SHE, demonstrated by the change from blue to red in regions in Figures 5E and 5F. The transition of Cu oxidation state from +1 to 0 from −0.8 to −1.0 V vs. SHE corroborates our previous finding regarding Cu intrinsic activity for NO_3RR to ammonia at larger overpotentials (−1.1 V vs. SHE, Figure 2A). Although we detect remaining Cu^+ species in the catalyst lattice in the maps constructed with XANES and XRF spectra, there is a clear direction that Cu oxidation states are transitioning to Cu^0 with applied negative potentials during NO_3RR, which is also confirmed by *in situ* Raman and punctual XANES spectra (Figures 5A and 5B).

We show with *in situ* Fourier transform infrared (FTIR) spectra that hydroxylamine (NH_2OH) is formed at −0.7 V vs. SHE and consumed at −1.0 V vs. SHE (Figure 5E) on Cu/Cu_2O catalyst surface, while on metallic Cu, it is formed at −0.9 V vs. SHE (Figure 5F). We detect the presence of hydroxylamine by tracking the peak centered at 1,111 cm^{-1}, attributed to -NH_2 stretch.[45] We highlight that Cu_2O reduction occurs at a less cathodic potential (−0.6 V vs. SHE, Figures 5A and 5B) than those under higher Faradaic efficiencies that were obtained for ammonia production (−0.77 to −1.1 V vs. SHE, Figure 2C). When metallic Cu is employed, hydroxylamine is only detected at −0.9 V vs. SHE (Figure 5F), which indicates that the presence of oxygen vacancies favors the formation of NH_2OH at a lower overpotential. This key role of previous Cu_2O reduction in NH_3 formation is also supported by the fact that we firstly detect hydroxylamine at −0.7 V vs. SHE, while Cu_2O reduces at −0.6 V vs. SHE (Figures 5A and 5B). We discuss in the next section how our attribution of the active sites' role is in context with the current literature.

Identifying the active sites of Cu/Cu_2O composites

Although several reports have hypothesized that the interface between Cu and Cu_2O is the active site for NO_3RR, our work indicates that under conditions where nitrate is converted to ammonia, Cu_2O is reduced and thus does not contribute to NO_3RR activity. Wang et al.[13] attributed the activity of CuO nanowires for NO_3RR to ammonia to the *in situ* formation of the interface between Cu and Cu_2O at cathodic potentials. Their work employed 0.5 mol L^{-1} Na_2SO_4 electrolyte and evaluated the catalyst performance for potentials from −0.55 to −0.95 V vs. RHE (−0.9 to −1.3 V vs. SHE, at reported initial pH), a similar potential range evaluated in our work. Shen et al.[21] also reported that the interface between Cu and Cu^+ species benefits NO_3RR to ammonia, since NO_3^- is firstly converted into NO_2^- on Cu active sites, and NO_2^- is reduced to NH_3 on Cu^+ sites. Using density functional theory (DFT), Wang et al.[13] proposed that the Cu-Cu_2O interface benefits the formation of *NOH that is further hydrogenated to form hydroxylamine. We demonstrate that these hydroxylamine species are formed at −0.7 V vs. SHE, a higher overpotential than the one at which the electrochemical reduction of Cu_2O occurs (−0.6 V vs. SHE). Combined with our observation that a pre-reduced Cu/Cu_2O catalyst has the same behavior as our as-prepared catalyst, we suggest that the Cu/Cu_2O interface is not responsible for the catalyst NO_3RR activity. Rather, we correlate the formation of oxygen vacancies from copper oxide to catalytic activity for NO_3RR to NH_3, supporting hypotheses in the literature.

Daiyan et al.[16] attribute the high activity of oxide-based catalysts for NO_3RR to ammonia to the presence of oxygen vacancies in the catalyst lattice, which is in

accordance with our results from −0.6 to −0.77 V vs. SHE. They employed DFT to demonstrate that oxygen vacancies favor the formation of the *HNO_2 intermediate that is further reduced to form *NO, *HNO, and *H_2NO intermediates. The formation of NH_3 occurs after the reduction of H_2NO* through a proton-electron pair transfer, which also forms *O. The results that we obtained from kinetic experiments agree with this hypothesis from −0.6 to −0.77 V vs. SHE. In this potential range, oxygen vacancies play an important role in stabilizing intermediate species that leads to ammonia formation. This is evidenced by higher NO_3^- rate orders and increased selectivity toward ammonia for the as-prepared and partially reduced catalysts (Figures 2C and 2D). However, we did not observe any enhanced activities and Faradaic efficiencies of oxygen vacancy-rich Cu/Cu_2O catalysts for overpotentials more negative than −0.77 V vs. SHE.

From −0.93 to −1.1 V vs. SHE, oxygen vacancies exhibit no positive effect on NH_3 formation from NO_3RR, in accordance with Li et al.,[18] who attribute the high activity and selectivity for NO_3RR to NH_3 of Cu nanotubes derived from CuO to the unique architecture and structure obtained from reduced copper oxides. Their work reported the optimal selectivity toward NH_3 at −1.3 V vs. SCE (approximately −1.0 V vs. SHE), which is the potential that our work recognizes that oxide-derived copper is more active than oxygen vacancies for NO_3RR to ammonia (Figure 2A). The higher activity of Cu obtained at larger overpotentials can be related to complete Cu_2O reduction at this potential range, leading to the inexistence of vacancies in these conditions. Furthermore, by comparing activities extracted from geometric and electrochemically active surface areas (Figure 2B), we demonstrate that when ECSA is considered, Cu has higher activity for ammonia at −1.1 V vs. SHE than our oxide-derived catalyst, while the opposite is found for geometric area, which can be attributed to the higher surface area of the Cu/Cu_2O catalysts.

In accordance with our findings, Zhou et al.[20] also reported a potential dependence on the active site of Cu_2O-based catalysts. They found that under potentials regimes more negative than −0.6 V vs. RHE (−1.0 V vs. SHE, at reported pH 7), oxide-derived copper is the active phase for NO_3RR to ammonia, while at lower overpotentials, the interface between Cu and Cu_2O is the active site that favors NO_2^- formation. We attribute the highest activity for NO_3RR to ammonia for pure copper active phases at −1.1 V vs. SHE. At −0.6 V vs. SHE, we detected the highest Faradaic efficiency toward nitrite (Figure S4), attributed to oxygen vacancies, since the reduction of Cu_2O was detected at this potential by *in situ* Raman and XANES spectra (Figures 5A and 5B). From kinetic experiments, we attribute to oxygen vacancies the enhanced NH_3 production at −0.77 V vs. SHE, which was not explored by Zhou and co-workers.[20] Thus, putting in context our findings with the current literature, we firstly demonstrated the potential dependence of Cu oxidation state and Cu_2O-based catalysts' active site for NO_3RR to NH_3 using kinetic, *ex situ*, and *in situ* characterizations.

Conclusions

Our work reveals a correlation between the active site of Cu/Cu_2O electrocatalysts and the applied potential employed for NO_3RR to ammonia. Copper oxide reduces at −0.6 V vs. SHE, and from −0.6 to −0.77 V vs. SHE, we attribute to oxygen vacancies on the catalyst surface the active site that boosts ammonia formation from NO_3RR. However, at higher overpotentials (−1.1 V vs. SHE), metallic copper itself is the active site, as demonstrated by comparison to metallic Cu and normalization to the ECSA. The pH of sodium sulfate electrolyte rapidly shifts from 5.8 to 11–12 during NO_3RR, which influences the mechanism that the reaction undergoes. When neutral PB electrolyte is employed at same initial pH conditions, the Faradaic

efficiency toward ammonia and nitrate rate orders are lower than the non-buffered one from −0.77 to −1.1 V vs. SHE, indicating that the alkalinization of the electrolyte improves the catalyst performance for NH_3 production at this potential window. These results highlight the need for catalyst characterization, ideally *in situ* or *operando* and kinetic analysis coupled to understand active sites. Additionally, careful control of the pH or its local measurement is necessary to understand the local environmental conditions during electrochemical reaction.

EXPERIMENTAL PROCEDURES

Resource availability

Lead contact

The lead contact of this work is Prof. Raphael Nagao (nagao@unicamp.br).

Materials availability

This study did not generate new reagents. Further information and requests for resources should be addressed to and fulfilled by the lead contact.

Data and code availability

Requests for data and resources should be addressed to and fulfilled by the lead contact.

Catalyst synthesis

The catalyst was electrodeposited using a one-compartment electrochemical cell. A gold layer (200 nm) on 10 nm of Ti that was deposited by electron beam onto a silicon wafer was used as substrate with 0.3848 cm^2 delimited area being the working electrode. A graphite rod was used as counter electrode and a single-junction Ag/AgCl as reference electrode. The electrolyte was prepared with 0.5 mol L^{-1} $CuSO_4.5H_2O$ (ACS reagent, >98.0%, Sigma-Aldrich) and 2.5 mol L^{-1} lactic acid (>85.0% Sigma-Aldrich), and the pH of the solution was adjusted to 9.0 with a 6.0 mol L^{-1} NaOH (ACS reagent, >97%, pellets, Sigma-Aldrich) solution.[29] The solution was stirred for at least 4 days after its preparation. The deposition was made by galvanostatic deposition at −0.75 mA cm^{-2}_{geo} for 1 h. Before each deposition, 10 scans of cyclic voltammetry were conducted between 0.1 and 0.6 V vs. SHE at scan rate of 50 mV s^{-1}. The underlying Au layer upon which the Cu was electrodeposited did not participate in the electrochemical reaction, as confirmed by controls of the Au substrate alone.

Electrochemical measurements

Electrolysis was conducted using a two-compartment electrochemical cell separated by a Nafion 117 membrane previously soaked in ultrapure water (resistivity >18.2 MΩ cm, Sinergy UV) for at least 1 day. Electrolyte contained 0.5 mol L^{-1} Na_2SO_4 (ACS reagent, >99.0%, anhydrous granular, Sigma-Aldrich) with the addition of different $NaNO_3$ (ReagentPlus, >99.0%, Sigma-Aldrich) concentrations in the catholyte. For the results reported with 0.2 mol L^{-1} PB, the electrolyte was prepared containing 22.08 g L^{-1} KH_2PO_4 (Certified ACS, Fisher Chemical) and 4.29 g L^{-1} Na_2HPO_4 (ACS reagent, >99.0%, Sigma-Aldrich). The alkalized Na_2SO_4 electrolyte was pH adjusted to 12 with 6 mol L^{-1} NaOH solution. pH was measured with the OrionStar A214, Thermo Scientific pHmeter. Argon was purged in the catholyte compartment at least 10 min before and during the electrolysis. All solutions were prepared with ultrapure water (resistivity >18.2 MΩ cm, Sinergy UV).

The working electrode (WE) for the as-prepared catalyst was obtained from the deposition previously described. 10-min- and 10-h-reduced catalysts were first submitted to a reduction at −1.0 V vs. SHE for the respective time in the same

electrochemical cell without nitrate. For pure Cu, a deposit of Cu (200 nm by electron beam) on Ti (10 nm) at a silicon wafer was used as WE, and it was submitted to a previous reduction step at −1.0 V vs. SHE for 10 min to reduce superficial oxides. A graphite rod was used as counter electrode and a single-junction Ag/AgCl as reference electrode. Electrolysis was conducted under potentiostatic regime for 10 min. Linear sweep voltammetries were conducted in the same setup from open circuit potential (0.1 V vs. SHE) to −1.2 V vs. SHE at 20 mV s^{-1} scan rate.

The potentials were corrected against standard hydrogen electrode (E_{SHE}) by the following equation:

$$E_{SHE} = E_{Ag/AgCl} + E^{0}_{Ag/AgCl}$$

Where $E_{Ag/AgCl}$ is the potential recorded against the Ag/AgCl reference electrode, and $E^{0}_{Ag/AgCl}$ is the standard potential of Ag/AgCl reference against SHE at 25°C. The value of $E^{0}_{Ag/AgCl}$ for the reference electrode used was 0.218 V vs. SHE based on calibration.

The potentials reported against reversible hydrogen electrode (E_{RHE}) were corrected by the following equation:

$$E_{RHE} = E_{Ag/AgCl} + E^{0}_{Ag/AgCl} + 0.059\ V\ pH$$

To account for series resistance, all electrochemical measurements were *iR*-compensated by 85% of the real component of the impedance measured at open circuit potential at 100 kHz, and the remaining 15% iR was corrected after the experiments. The catholyte solution was stirred at 700 rpm and carried out using a Biologic SP−150 potentiostat.

Colorimetric quantification methods

NH_3 quantification was conducted using the indophenol blue method. The protocol consists of mixing 3 mL of the sample with 500 μL of a solution containing 0.4 mol L^{-1} sodium salicylate (ACS reagent, >99%, Sigma-Aldrich), 0.32 mol L^{-1} NaOH (ACS reagent, >97%, pellets, Sigma-Aldrich), 50 μL of 1% (w/w) sodium nitroprusside dihydrate (ACS reagent, >99.0%), and 50 μL of sodium hypochlorite solution (reagent grade, available chlorine 4.00%–4.99%). UV-vis spectra were measured from 500 to 800 nm using Evolution 350 UV-Vis (Thermo Scientific), and the absorbance used for quantification was 657 nm[46]

Nitrite quantification was carried out using the Griess method. 500 μL of the sample was mixed with 2.5 mL of water and 500 μL of Griess reagent, which consists of the dissolution of 0.1 g of *N*-(1-naphthyl)ethylenediamine hydrochloride (ACS reagent, >98%, Sigma-Aldrich), 1.0 g of sulfanilamide (Fisher Chemical), and 2.94 mL of H_2PO_4 (ACS reagent, >85%, Sigma-Aldrich) in 50 mL of ultrapure water. UV-vis spectra were measured from 400 to 800 nm using Evolution 350 UV-Vis (Thermo Scientific), and the absorbance used for quantification was 540 nm[46]

Calculation of Faradaic efficiencies and partial current densities

Faradaic efficiencies (FEs) were calculated from the following equation:

$$FE = \frac{n \bullet F \bullet [P] \bullet V_{cat}}{Q_{total}} \bullet 100\%$$

Here, n is the number of electrons transferred (8 for NH_3 and 2 for NO_2^-), F the Faraday constant (96,485 C mol^{-1}), [P] either ammonia or nitrite concentration in

mol L^{-1}, V_{cat} the catholyte volume (0.04 L), and Q_{total} the total charge after the electrolysis.

Partial current density (j_{NH3}) was obtained from the product of *FE* and the steady-state current density recorded at the end of the electrolysis. The current densities were normalized by ECSA obtained after the electrolysis.

Electrochemically active surface area measurements

ECSA was measured by obtaining the double-layer capacitance from the slope of the linear relationship between the current recorded at open circuit potential (OCP) of cyclic voltammetries obtained from −50 to 50 mV vs. OCP and the scan rate (10–100 mV s^{-1}).[13] Then, the ECSA is calculated by the following:

$$ECSA = \frac{C_{dl}}{C_{specific}}$$

Here, C_{dl} is the double-layer capacitance and $C_{specific}$ the Cu-specific capacitance, which was calculated by the division of C_{dl} measured for a flat, pure copper plate (200 nm) on Ti (10 nm) at silicon wafer and its geometric surface area (0.3848 cm^2).

Scanning electron microscopy

We obtained scanning electron microscopy images were obtained using Quanta 650 FEG microscope by detection of secondary electrons by Everhart-Thornley detector, employing 20.0 kV, with a working distance of 6.0 mm and horizontal field of 2.98 μm.

Transmission electron microscopy

We obtained TEM images with a JEOL JEM-2100 microscope equipped with LaB_6 electron gun and accelerating voltage of 200 kV for both TEM and STEM modes, with spatial resolutions of 0.25 nm and 1 nm respectively.

Atomic force microscopy

AFM maps were recorded using the NX10-ParkSystems equipment. We used the AFM tip from NanoSensors recovered with Pt/Ir, with a spring constant of 2.8 N m^{-2} and resonance frequency of 75 kHz. The scanned area was 25 μm^2.

X-ray photoelectron spectroscopy

We obtained XPS spectra with a Thermo Scientific K-α X-ray excited photoelectron spectrometer. The spectra were acquired from 10 scans for a total time of 3 min and 20.5 s, Al K-α gun source, spot size of 300 μm, pass energy of 50.0 eV, and energy step size of 0.100 eV.

In situ Raman spectroscopy

In situ Raman spectroscopy was performed with a Renishaw InVia microscope, with a 633-nm laser. The spectro-electrochemical cell was assembled on top of a quartz window, in a three-electrode configuration cell: Cu/Cu_2O deposited on Au (0.3848 cm^2) as working electrode (WE), a platinum wire as counter electrode (CE), and a leakless Ag/AgCl as reference electrode (RE) (Figure S1C). *In situ* Raman spectra were obtained by the accumulation of 16 scans, with 100% laser power, 1-s exposure time, at the selected potentials. The spectra were collected during chronoamperometry measurements with electrolyte containing 0.5 mol L^{-1} Na_2SO_4 with and without 0.1 mol L^{-1} $NaNO_3$ from 0.0 to −1.0 V vs. SHE (at every 100 mV) using a WaveNow potentiostat from Pine Research.

In situ X-ray fluorescence, absorption, and spectromicroscopy

Synchrotron experiments were carried out at beamline Carnaúba/Sirius, at Tarumã station, using a beam size of 200 × 500 nm^2 (nanoprobe) with an estimated flux of about 10^9 photons/second on the sample. X-ray fluorescence mapping (nano-XRF) was carried out in continuous scan mode (called flyscan) over 50 × 50 μm with a step size of 500 nm (pixel size) by scanning the sample.[44] Punctual *in situ* X-ray absorption spectroscopy experiments were performed using a four-bounce Si (111) monochromator with energy resolution of 10^{-4} keV at step of 0.5 eV. Combining XRF and energy scan, XANES maps were obtained by acquiring XRF images from 8,974 eV to 9,000 eV in steps of 0.5 eV, in which the stack of all XRF maps leads to the XANES map, where each pixel corresponds to a XANES spectrum. The concentration maps were obtained using an in-house development: the CORAL (curve resolution for data analysis), which is based in PCA.[47] The punctual spectra and XANES maps were collected during chronoamperometry measurements with electrolyte containing 0.5 mol L^{-1} Na_2SO_4 and 0.1 mol L^{-1} $NaNO_3$ from −0.4 to −1.0 V vs. SHE (at every 100 mV) using a EC301 potentiostat from Stanford Research Systems.

In situ Fourier transform infrared spectroscopy

In situ FTIR was performed with a Shimadzu IR prestige-21 spectrometer equipped with a mercury-cadmium-telluride detector refrigerated with liquid nitrogen. The spectro-electrochemical cell (SEC) was assembled on top of a CaF_2 window and positioned on the upper part of a specular reflection accessory (Pike Technologies, model VeeMax II) (Figure S1B). The SEC worked in a three-electrode configuration cell, composed of a platinum wire with a cylindrical end and an RHE as the CE and RE, respectively. As WE, Cu_2O/Cu was electrodeposited onto a gold disk (d = 0.5 cm). To form a thin layer, the WEs were assembled into the cell and carefully pressed against the transparent FTIR window. The SEC was controlled by a PGSTAT 204 potentiostat (Autolab), and the FTIR spectra were obtained by external reflection from an average of 128 scans with a resolution of 8 cm^{-1} at the selected potentials. The spectra were collected during chronoamperometry measurements in 0.5 M Na_2SO_4 and 24 mM $NaNO_3$ from −0.3 to −1.2 V vs. SHE (at every 100 mV) and compared to the reference potential (−0.35 V vs. SHE).

Nuclear magnetic resonance

In order to perform ^1H nuclear magnetic resonance (NMR) analysis of NH_4^+ species, the samples were prepared as follows. First, all NH_3 produced after 1 h of electrolysis at −0.8 V vs. SHE was acidified for pH = 3, to ensure that all NH_3 was converted to NH_4^+. Then, 550 μL was transferred to a 5-mm NMR tube and 100 μL D_2O was added to adjust the lock of the spectrometer. The ^1H NMR measurements were performed at room temperature on a Bruker AVANCE III NMR spectrometer, operating at 11.7 Tesla, observing ^1H nuclei at 500.13 MHz. The instrument was equipped with a direct detection probe.

For the ^{15}N isotope-labeling experiment, $Na^{15}NO_3$ (98 atom% ^{15}N) was used as a reactant, to elucidate the real source of NH_3 formation in nitrate reduction reaction. For ^{15}N, the methods for electrolysis, sample preparation, and NMR analysis were the same employed for ^{14}N.

The spectra of ^{1}NMR were acquired using pulse sequence *zgesgp* (Bruker library) using the following parameters: 2-s relaxation delay (d1), four dummy scans (ds), 1,000 transients (ns), 4.089 s acquisition time, and 64,000 data points distributed over 8,012 Hz spectral width. The spectra were processed by the application of an exponential multiplication-free induction decay with a line broadening factor of 0.3 Hz, followed by Fourier transform with zero filling by a factor of 2.

SUPPLEMENTAL INFORMATION

Supplemental information can be found online at https://doi.org/10.1016/j.checat.2023.100850.

ACKNOWLEDGMENTS

The authors acknowledge support from Fundação de Amparo à Pesquisa do Estado de São Paulo (FAPESP) process numbers: G.F.C., 2019/18847-6, 2022/01799-1; M.R.P., 2019/08244-2; and R.N., 2023/02841-4, 2022/14169-6, 2021/08868-6. M.W., T.M., and R.N. acknowledge Shell-CINE (Center for Innovation on New Energies; Division 1: Dense Energy Carriers) (2017/11986-5). I.M. acknowledges Coordenação de Aperfeiçoamento de Pessoal de Nível Superior (CAPES) grant number 88887.339501/2019-00. N.S. acknowledges support from NSF grant no. 2247194. This research used resources of the Brazilian Synchrotron Light Laboratory (LNLS) and Brazilian Nanotechnology National Laboratory (LNNano), both part of the Brazilian Center for Research on Energy and Materials (CNPEM), a private non-profit organization under the supervision of the Brazilian Ministry for Science, Technology, and Innovations (MCTI). The Carnaúba beamline staff are acknowledged for their assistance during the experiments.

AUTHOR CONTRIBUTIONS

G.F.C. wrote the manuscript and conducted all synthesis, kinetic, and *in situ* Raman experiments. M.W. conducted *in situ* FTIR spectroscopy measurements. G.F.C., M.W., T.M., and I.T.N. conducted and/or discussed *in situ* XANES and XRF spectromicroscopy results. M.R.P. assisted with the catalyst synthesis and discussed characterization data. I.M. contributed to discussing electrolysis experiments. J.B.S.J. conducted *ex situ* microscopic and spectroscopic experiments. M.F.C.S. and C.F.T. conducted and discussed NMR results. N.S. and R.N. conceptualized and supervised the project. All the authors contributed to discussions and the writing of the manuscript.

DECLARATION OF INTERESTS

The authors declare no conflicts of interest.

Received: September 26, 2023
Revised: November 28, 2023
Accepted: November 29, 2023
Published: December 22, 2023

REFERENCES

1. Galloway, J.N., Aber, J.D., Erisman, J.W., Seitzinger, S.P., Howarth, R.W., Cowling, E.B., and Cosby, B.J. (2003). The nitrogen cascade. Bioscience *53*, 341–356.

2. Zeng, Y., Priest, C., Wang, G., and Wu, G. (2020). Restoring the Nitrogen Cycle by Electrochemical Reduction of Nitrate: Progress and Prospects. Small Methods *4*.

3. Schiffer, Z.J., and Manthiram, K. (2017). Electrification and Decarbonization of the Chemical Industry. Joule *1*, 10–14.

4. Fields, S. (2004). Global Nitrogen: Cycling out of Control. Environ. Health Perspect. *112*, A556–A563.

5. Wang, Z., Richards, D., and Singh, N. (2021). Recent discoveries in the reaction mechanism of heterogeneous electrocatalytic nitrate reduction. Catal. Sci. Technol. *11*, 705–725.

6. Singh, N., and Goldsmith, B.R. (2020). Role of Electrocatalysis in the Remediation of Water Pollutants. ACS Catal. *10*, 3365–3371.

7. van Langevelde, P.H., Katsounaros, I., and Koper, M.T. (2021). Electrocatalytic Nitrate Reduction for Sustainable Ammonia Production. Joule *5*, 290–294.

8. Cerrón-Calle, G.A., Senftle, T.P., and Garcia-Segura, S. (2022). Strategic tailored design of electrocatalysts for environmental remediation based on density functional theory (DFT) and microkinetic modeling. Curr. Opin. Electrochem. *35*, 101062.

9. Teng, M., Ye, J., Wan, C., He, G., and Chen, H. (2022). Research Progress on Cu-Based Catalysts for Electrochemical Nitrate Reduction Reaction to Ammonia. Ind. Eng. Chem. Res. *61*, 14731–14746.

10. Jung, W., and Hwang, Y.J. (2021). Material strategies in the electrochemical nitrate reduction reaction to ammonia production. Mater. Chem. Front. *5*, 6803–6823.

11. Garcia-Segura, S., Lanzarini-Lopes, M., Hristovski, K., and Westerhoff, P. (2018). Electrocatalytic reduction of nitrate: Fundamentals to full-scale water treatment applications. Appl. Catal., B *236*, 546–568.

12. Roy, C., Deschamps, J., Martin, M.H., Bertin, E., Reyter, D., Garbarino, S., Roué, L., and Guay, D. (2016). Identification of Cu surface active sites

for a complete nitrate-to-nitrite conversion with nanostructured catalysts. Appl. Catal., B *187*, 399–407.

13. Wang, Y., Zhou, W., Jia, R., Yu, Y., and Zhang, B. (2020). Unveiling the Activity Origin of a Copper-based Electrocatalyst for Selective Nitrate Reduction to Ammonia. Angew. Chem. Int. Ed. *59*, 5350–5354.

14. Zhao, J., Shen, Z., Yu, J., Guo, Y., Mushtaq, M.A., Ding, Y., Song, Z., Zhang, W., Huang, X., Li, Y., et al. (2022). Constructing Cu-CuO heterostructured skin on Cu cubes to promote electrocatalytic ammonia production from nitrate wastewater. J. Hazard Mater. *439*, 129653.

15. Yin, H., Zhao, X., Xiong, S., Peng, Y., Chen, Z., Wang, R., Wen, M., Luo, J., Yamashita, H., and Li, J. (2022). New insight on electroreduction of nitrate to ammonia driven by oxygen vacancies-induced strong interface interactions. J. Catal. *406*, 39–47.

16. Daiyan, R., Tran-Phu, T., Kumar, P., Iputera, K., Tong, Z., Leverett, J., Khan, M.H.A., Asghar Esmailpour, A., Jalili, A., Lim, M., et al. (2021). Nitrate reduction to ammonium: From CuO defect engineering to waste NOx-to-NH3 economic feasibility. Energy Environ. Sci. *14*, 3588–3598.

17. Yuan, J., Xing, Z., Tang, Y., and Liu, C. (2021). Tuning the Oxidation State of Cu Electrodes for Selective Electrosynthesis of Ammonia from Nitrate. ACS Appl. Mater. Interfaces *13*, 52469–52478.

18. Li, C., Liu, S., Xu, Y., Ren, T., Guo, Y., Wang, Z., Li, X., Wang, L., and Wang, H. (2022). Controllable reconstruction of copper nanowires into nanotubes for efficient electrocatalytic nitrate conversion into ammonia. Nanoscale *14*, 12332–12338.

19. Song, Z., Liu, Y., Zhong, Y., Guo, Q., Zeng, J., and Geng, Z. (2022). Efficient Electroreduction of Nitrate into Ammonia at Ultralow Concentrations Via an Enrichment Effect. Adv. Mater. *34*, e2204306.

20. Zhou, N., Wang, Z., Zhang, N., Bao, D., Zhong, H., and Zhang, X. (2023). Potential-Induced Synthesis and Structural Identification of Oxide-Derived Cu Electrocatalysts for Selective Nitrate Reduction to Ammonia. ACS Catal. *13*, 7529–7537.

21. Shen, Z., Yan, J., Wang, M., Xing, L., Huang, B., Zhou, H., Li, W., Chen, L., and Shi, J. (2023). Cu/Cu^{+} Synergetic Effect in Cu_2O/Cu/CF Electrocatalysts for Efficient Nitrate Reduction to Ammonia. ACS Sustain. Chem. Eng. *11*, 9433–9441.

22. Anastasiadou, D., van Beek, Y., Chen, W., Wissink, T., Parastaev, A., Hensen, E.J.M., and Costa Figueiredo, M. (2023). Morphology Changes of Cu_2O Catalysts During Nitrate Electroreduction to Ammonia. ChemCatChem *15*.

23. Ren, T., Yu, Z., Yu, H., Deng, K., Wang, Z., Li, X., Wang, H., Wang, L., and Xu, Y. (2022). Interfacial polarization in metal-organic framework reconstructed Cu/Pd/CuOx multi-phase heterostructures for electrocatalytic nitrate reduction to ammonia. Appl. Catal., B *318*, 121805.

24. Cerrón-Calle, G.A., Wines, A., and Garcia-Segura, S. (2023). Atomic hydrogen provision by cobalt sites in a bimetallic Ni/Co(OH)x and trimetallic Ni/Cu2O/Co(OH)x configurations for superior ammonia production. Appl. Catal., B *328*, 122540.

25. Wang, J., Chen, H.-C., Tan, H.-Y., Tan, C.M., Zhu, Y., and Chen, H.M. (2022). Strong Correlation between the Dynamic Chemical State and Product Profile of Carbon Dioxide Electroreduction. ACS Appl. Mater. Interfaces *14*, 22681–22696.

26. Mom, R.V., Velasco-Velez, J.J., Sandoval-Diaz, L.E., Falling, L.J., Chuang, C.H., Gao, D., Jones, T.E., Zhu, Q., Arrigo, R., Roldan Cuenya, B., et al. (2020). Revealing the Active Phase of Copper during the Electroreduction of CO2in Aqueous Electrolyte by Correlating in Situ X-ray Spectroscopy and in Situ Electron Microscopy. ACS Energy Lett. *5*, 2106–2111.

27. Wang, J., Tan, H.Y., Zhu, Y., Chu, H., and Chen, H.M. (2021). Linking the Dynamic Chemical State of Catalysts with the Product Profile of Electrocatalytic CO_2 Reduction. Angew. Chem. Int. Ed. *60*, 17254–17267.

28. Fajardo, A.S., Westerhoff, P., Sanchez-Sanchez, C.M., and Garcia-Segura, S. (2021). Earth-abundant elements a sustainable solution for electrocatalytic reduction of nitrate. Appl. Catal., B *281*, 119465.

29. Pinto, M.R., Pereira, G.B., Queiroz, A.C., and Nagao, R. (2020). Influence of the Ligands in Cu(II) Complexes on the Oscillatory Electrodeposition of Cu/Cu2O. J. Phys. Chem. C *124*, 12559–12568.

30. Kitagaki, B.T., Pinto, M.R., Queiroz, A.C., Breitkreitz, M.C., Rossi, F., and Nagao, R. (2019). Multivariate statistical analysis of chemical and electrochemical oscillators for an accurate frequency selection. Phys. Chem. Chem. Phys. *21*, 16423–16434.

31. Switzer, J.A., Hung, C.-J., Huang, L.-Y., Miller, F.S., Zhou, Y., Raub, E.R., Shumsky, M.G., and Bohannan, E.W. (1998). Potential oscillations during the electrochemical self-assembly of copper/cuprous oxide layered nanostructures. J. Mater. Res. *13*, 909–916.

32. Kim, S.J., Kim, S., Lee, J., Jo, Y., Seo, Y.S., Lee, M., Lee, Y., Cho, C.R., Kim, J.P., Cheon, M., et al. (2021). Color of Copper/Copper Oxide. Adv. Mater. *33*, e2007345.

33. Jia, R., Wang, Y., Wang, C., Ling, Y., Yu, Y., and Zhang, B. (2020). Boosting Selective Nitrate Electroreduction to Ammonium by Constructing Oxygen Vacancies in TiO2. ACS Catal. *10*, 3533–3540.

34. Fajardo, A.S., Westerhoff, P., Garcia-Segura, S., and Sánchez-Sánchez, C.M. (2023). Selectivity modulation during electrochemical reduction of nitrate by electrolyte engineering. Sep. Purif. Technol. *321*, 124233.

35. Kas, R., Yang, K., Bohra, D., Kortlever, R., Burdyny, T., and Smith, W.A. (2020). Electrochemical CO_2 reduction on nanostructured metal electrodes: fact or defect? Chem. Sci. *11*, 1738–1749.

36. Jung, S., McCrory, C.C.L., Ferrer, I.M., Peters, J.C., and Jaramillo, T.F. (2016). Benchmarking nanoparticulate metal oxide electrocatalysts for the alkaline water oxidation reaction. J. Mater. Chem. A Mater. *4*, 3068–3076.

37. Pérez-Gallent, E., Figueiredo, M.C., Katsounaros, I., and Koper, M.T. (2017). Electrocatalytic reduction of Nitrate on Copper single crystals in acidic and alkaline solutions. Electrochim. Acta *227*, 77–84.

38. Hu, Q., Qin, Y., Wang, X., Zheng, H., Gao, K., Yang, H., Zhang, P., Shao, M., and He, C. (2022). Grain Boundaries Engineering of Hollow Copper Nanoparticles Enables Highly Efficient Ammonia Electrosynthesis from Nitrate. CCS Chem. *4*, 2053–2064.

39. Frankcombe, T.J., and Liu, Y. (2023). Interpretation of Oxygen 1s X-ray Photoelectron Spectroscopy of ZnO. Chem. Mater. *35*, 5468–5474.

40. Gao, S., Sun, Z., Liu, W., Jiao, X., Zu, X., Hu, Q., Sun, Y., Yao, T., Zhang, W., Wei, S., and Xie, Y. (2017). Atomic layer confined vacancies for atomic-level insights into carbon dioxide electroreduction. Nat. Commun. *8*, 14503.

41. Deng, Y., Handoko, A.D., Du, Y., Xi, S., and Yeo, B.S. (2016). In Situ Raman Spectroscopy of Copper and Copper Oxide Surfaces during Electrochemical Oxygen Evolution Reaction: Identification of Cu III Oxides as Catalytically Active Species. ACS Catal. *6*, 2473–2481.

42. Gaur, A., Shrivastava, D., and Joshi, K. (2009). Copper K-edge XANES of Cu(I) and Cu(II) oxide mixtures. In Journal of Physics: Conference Series (Institute of Physics Publishing).

43. Guda, A.A., Guda, S.A., Martini, A., Kravtsova, A.N., Algasov, A., Bugaev, A., Kubrin, S.P., Guda, L.V., Šot, P., van Bokhoven, J.A., et al. (2021). Understanding X-ray absorption spectra by means of descriptors and machine learning algorithms. npj Comput. Mater. *7*, 203.

44. Vicente, R.A., Raju, S.P., Gomes, H.V.N., Neckel, I.T., Tolentino, H.C.N., and Fernández, P.S. (2023). Development of Electrochemical Cells and Their Application for Spatially Resolved Analysis Using a Multitechnique Approach: From Conventional Experiments to X-Ray Nanoprobe Beamlines. Anal. Chem. *95*, 16144–16152.

45. Liu, H., Lang, X., Zhu, C., Timoshenko, J., Rüscher, M., Bai, L., Guijarro, N., Yin, H., Peng, Y., Li, J., et al. (2022). Efficient Electrochemical Nitrate Reduction to Ammonia with Copper-Supported Rhodium Cluster and Single-Atom Catalysts. Angew. Chem. Int. Ed. *61*, e202202556.

46. Chen, G.F., Yuan, Y., Jiang, H., Ren, S.Y., Ding, L.X., Ma, L., Wu, T., Lu, J., and Wang, H. (2020). Electrochemical reduction of nitrate to ammonia via direct eight-electron transfer using a copper–molecular solid catalyst. Nat. Energy *5*, 605–613.

47. Figueroa, S.J., Rochet, A., Ferreira Torquato, I., Espíndola, A.M., Rigamonti, H., Meyer, B.C., and Azevedo, G.d.M. (2023). QUATI beamline: QUick x-ray Absorption spectroscopy for TIme and space-resolved experiments at the Brazilian Synchrotron Light Laboratory. Radiat. Phys. Chem. *212*, 111198.